nature physics

LETTERS

https://doi.org/10.1038/s41567-021-01326-9

Check for updates

OPEN

Mass measurements of $^{99-101}$In challenge ab initio nuclear theory of the nuclide ^{100}Sn

M. Mougeot[1,2]✉, D. Atanasov[2], J. Karthein[1,2,17], R. N. Wolf[3], P. Ascher[4], K. Blaum[1], K. Chrysalidis[2], G. Hagen[5,6], J. D. Holt[7,8], W. J. Huang[1,18], G. R. Jansen[9], I. Kulikov[10], Yu. A. Litvinov[10], D. Lunney[11], V. Manea[2,11], T. Miyagi[7], T. Papenbrock[5,6], L. Schweikhard[12], A. Schwenk[1,13,14], T. Steinsberger[1], S. R. Stroberg[15], Z. H. Sun[5,6], A. Welker[2], F. Wienholtz[2,12,13], S. G. Wilkins[2] and K. Zuber[16]

The tin isotope ^{100}Sn is of singular interest for nuclear structure due to its closed-shell proton and neutron configurations. It is also the heaviest nucleus comprising protons and neutrons in equal numbers—a feature that enhances the contribution of the short-range proton–neutron pairing interaction and strongly influences its decay via the weak interaction. Decay studies in the region of ^{100}Sn have attempted to prove its doubly magic character[1] but few have studied it from an ab initio theoretical perspective[2,3], and none of these has addressed the odd-proton neighbours, which are inherently more difficult to describe but crucial for a complete test of nuclear forces. Here we present direct mass measurements of the exotic odd-proton nuclide ^{100}In, the beta-decay daughter of ^{100}Sn, and of ^{99}In, with one proton less than ^{100}Sn. We use advanced mass spectrometry techniques to measure ^{99}In, which is produced at a rate of only a few ions per second, and to resolve the ground and isomeric states in ^{101}In. The experimental results are compared with ab initio many-body calculations. The 100-fold improvement in precision of the ^{100}In mass value highlights a discrepancy in the atomic-mass values of ^{100}Sn deduced from recent beta-decay results[4,5].

The nuclear landscape is shaped by the underlying strong, weak and electromagnetic forces. The most salient features are the pillars of enhanced differential binding energy associated with closed-shell configurations, the best example of which is $Z=50$ (tin), featuring the largest number of β-stable isotopes (10) of all elements. These nuclides lie between the closed neutron shells $N=50$ and 82, conferring particular importance to the nuclides ^{100}Sn and ^{132}Sn. The neutron-rich ^{132}Sn can be synthesized in comfortable quantities[6]. This is not so for ^{100}Sn, forming the limit of proton stability due to its extreme neutron deficiency, only just staving off the Coulomb repulsion of the 50 protons. This rare combination of like closed shells causes ^{100}Sn to have one of the strongest beta transitions and makes it the heaviest self-conjugate nucleus on the nuclear chart.

Nuclei in the immediate vicinity of ^{100}Sn offer important insight for understanding the single-neutron and proton states in this region and constitute an excellent proxy for the study of ^{100}Sn itself. However, experiments have so far only been feasible with in-beam gamma-ray spectroscopy at fragmentation facilities[4,5,7–10]. By direct determination of the nuclear binding energy, high-precision atomic-mass measurements provide a crucial model-independent probe of the structural evolution of exotic nuclei. Precision mass measurements are traditionally performed at isotope separation online (ISOL) facilities; however, the production of medium-mass, neutron-deficient nuclides at such facilities is prohibitively difficult, explaining the lack of accurate mass values in the region. Measurements performed at the FRS Ion Catcher at GSI[11] and the Cooler-Storage experimental Ring (CSRe) in Langzhou[12] (both high-energy, heavy-ion fragmentation facilities) recently extended direct mass measurements to the ^{101}In ground and isomeric states. However, the ^{100}In mass value is still constrained 63% indirectly through its beta-decay link to ^{100}Cd (ref. [13]).

Thus, the first experimental challenge overcome in this work was the production and separation of the successfully studied ^{99,100,101g,101m}In states. A detailed schematic of the necessary stages, from radioactive ion beam production to beam purification, preparation and measurement, is shown in Fig. 1. The exotic indium isotopes were produced at the Isotope Separator On Line Device (ISOLDE) located at CERN. A 1.4 GeV proton beam impinged on a thick lanthanum carbide target, producing a swath of neutron-deficient radioactive species of various chemical elements. After diffusion from the heated target, the indium atoms of interest were selectively ionized using a two-step resonance laser ionization scheme provided by the ISOLDE Resonant Ionization Laser Ion Source (RILIS)[14]. The ion beam was extracted from the source and accelerated to an energy of 40 keV. The mass number ($A=Z+N$) of interest was selected using ISOLDE's high-resolution dipole mass separator and delivered to the ISOLTRAP online mass spectrometer[15].

[1]Max-Planck-Institut für Kernphysik, Heidelberg, Germany. [2]CERN, Geneva, Switzerland. [3]ARC Centre of Excellence for Engineered Quantum Systems, School of Physics, The University of Sydney, Sydney, New South Wales, Australia. [4]Centre d'Etudes Nucléaires de Bordeaux Gradignan, UMR 5797 CNRS/IN2P3, Université de Bordeaux, Gradignan, France. [5]Physics Division, Oak Ridge National Laboratory, Oak Ridge, TN, USA. [6]Department of Physics and Astronomy, University of Tennessee, Knoxville, TN, USA. [7]TRIUMF, Vancouver, British Columbia, Canada. [8]Department of Physics, McGill University, Montreal, Quebec, Canada. [9]National Center for Computational Sciences, Oak Ridge National Laboratory, Oak Ridge, TN, USA. [10]GSI Helmholtzzentrum für Schwerionenforschung GmbH, Darmstadt, Germany. [11]CNRS/IN2P3, IJCLab, Université Paris-Saclay, Orsay, France. [12]Institut für Physik, Universität Greifswald, Greifswald, Germany. [13]Department of Physics, Technische Universität Darmstadt, Darmstadt, Germany. [14]ExtreMe Matter Institute EMMI, GSI Helmholtzzentrum für Schwerionenforschung GmbH, Darmstadt, Germany. [15]Physics Department, University of Washington, Seattle, WA, USA. [16]Technische Universität Dresden, Dresden, Germany. [17]Present address: Massachusetts Institute of Technology, Cambridge, MA, USA. [18]Present address: Advanced Energy Science and Technology Guangdong Laboratory, Huizhou, China. ✉e-mail: maxime.mougeot@cern.ch

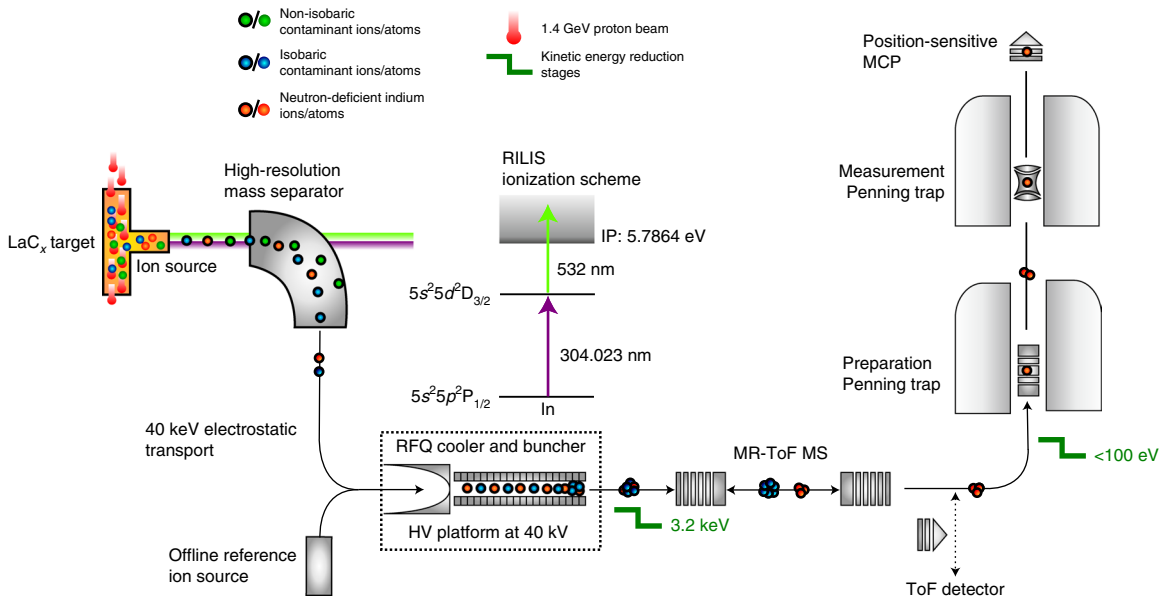

Fig. 1 | High-precision mass measurements of neutron-deficient indium isotopes with ISOLTRAP. Radioactive atoms were produced by nuclear reactions of 1.4 GeV protons impinging on a thick lanthanum carbide target. Short-lived indium atoms diffusing from the target were selectively ionized using a two-step laser excitation scheme, provided by the ISOLDE RILIS, which excited one electron above the indium ionization potential (IP). The extracted ion beam was mass separated and injected into a radiofrequency quadrupole (RFQ) ion trap sitting on a high-voltage (HV) platform, where it was bunched and cooled. The beam was then processed by an MR-ToF MS to separate the indium ions from the isobaric contaminants. When the precision Penning trap was used for the mass measurement, further cooling and purification of the beam was achieved using a helium buffer-gas-filled preparation Penning trap. A position-sensitive microchannel plate (MCP) detector was used to record the time of flight and/or the position of the ion after ejection from the precision Penning trap. In the case of ^{99}In, for which the production yield was too low, the MR-ToF MS was used to perform the mass measurement. Reference alkali ions were provided by the ISOLTRAP offline ion source (see text for details).

The ions were first accumulated in ISOLTRAP's linear radio-frequency quadrupole cooler and buncher trap[16]. The extracted bunches were subsequently decelerated by a pulsed drift cavity to an energy of 3.2 keV before being purified by the multireflection time-of-flight mass spectrometer (MR-ToF MS)[17], where multiple passages between two electrostatic mirrors rapidly separate the short-lived indium ions from much more abundant molecules of approximately the same mass. For all investigated isotopes, surviving molecular ions $^{80-82}$Sr^{19}F$^+$ were predominant in the ISOLDE beam. After a typical trapping time of about 25 ms, a resolving power in excess of $m/\Delta m = 10^5$ was achieved. This combination of speed and high resolving power enables the MR-ToF MS to perform precise mass measurements of very short-lived species (Methods). Because of its low production yield of <10 ions per second, the mass of ^{99}In was measured with this latter method only (see typical MR-ToF MS spectrum in Fig. 2).

The rate of ^{100}In and ^{101}In behind the MR-ToF MS was sufficient to perform Penning-trap mass measurements. For ^{100}In the conventional time-of-flight ion-cyclotron-resonance (ToF-ICR) technique was used (Methods and Extended Data Fig. 1). Even-N neutron-deficient indium isotopes are known to exhibit long-lived isomeric states lying a few hundred kiloelectron-volts above the corresponding ground state, owing to the close energy proximity between the $\pi g_{9/2}$ and $\pi p_{1/2}$ states and their large spin difference. As a result, the $A = 101$ indium beam delivered to ISOLTRAP was a mixture of two such states, so the phase-imaging ion-cyclotron-resonance (PI-ICR) technique[18,19] had to be used to resolve them and ensure the accuracy of the ground-state mass value (Methods and Extended Data Fig. 1 for more details).

Table 1 summarizes our experimental results and compares them with the literature. The ISOLTRAP mass values for the ground and isomeric states of ^{101}In agree well with averages obtained from refs. [11,12]. The excitation energy is determined to be 668(11) keV, reducing the uncertainty by a factor of four. The ToF-ICR measurement of ^{101g}In is in excellent agreement with the value measured using PI-ICR. ^{100}In is found to be 130 keV more bound, while the mass uncertainty is improved by almost a factor of 90.

Since the ^{100}Sn 2016 Atomic-Mass Evaluation (AME2016) mass excess value of −57,280(300) keV (ref. [20]) is derived from that of ^{100}In and the β-decay energy of ref. [4], our ^{100}In result improves the ^{100}Sn mass excess to −57,148(240) keV. However, combining our result with the more recently published β-decay Q-value (that is, the energy released in the decay) from ref. [5] yields a ^{100}Sn mass excess of −56,488(160) keV. For both decay energies, the ^{100}Sn mass is found to be more bound than previously inferred. In addition, the almost 2 s.d. between the Q-values from refs. [4,5] yields ^{100}Sn mass values that differ by 650 keV. We examine the consequences below and resolve this inconsistency.

Because the binding energy is a large quantity, finite differences are commonly used for assessing changes in nuclear structure from the mass surface. Shown in Fig. 2 (open grey symbols) is the two-neutron empirical shell gap defined as $\Delta_{2n}(Z,N_0) = M_E(Z,N_0-2) - 2M_E(Z,N_0) + M_E(Z,N_0+2)$, where $M_E(Z,N_0) = M_{atomic}(Z,N_0) - (Z+N_0)\times u$ (atomic mass unit) is the mass excess of a nucleus with Z protons and a magic neutron number N_0. It shows a local maximum at the crossing of a magic proton number, a phenomenon known as 'mutually enhanced magicity'[21].

Since the lack of mass data for the $N = 48$ isotopes of In ($Z = 49$), Cd ($Z = 48$) and Ag ($Z = 47$) prevents derivation of this quantity out to ^{100}Sn, we adapt an approach proposed in ref. [22] using $\Delta_{2n}(Z,N_0+2)$, which is inversely correlated to $\Delta_{2n}(Z,N_0)$ (filled grey symbols in Fig. 2c). With this difference, a local minimum is observed because the binding energy of the magic neutron number appears in $\Delta_{2n}(Z,N_0+2)$ with opposite sign. The case of $N = 28$

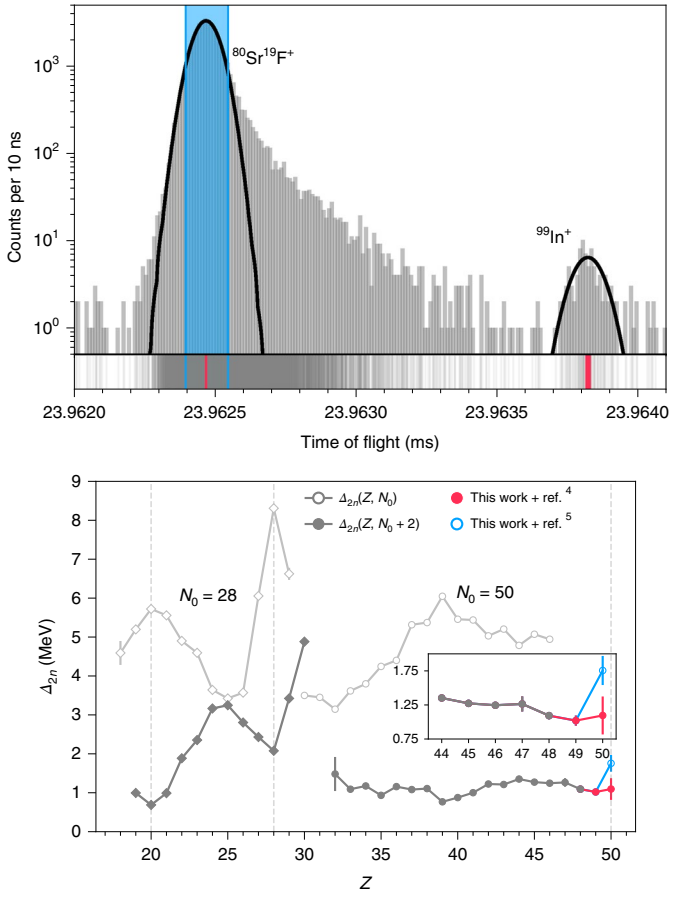

Fig. 2 | Overview of the experimental results. Top: a typical $A=99$ MR-ToF MS spectrum obtained after 1,000 revolutions. The solid black lines represent the Gaussian fit probability density function scaled to the histogram within the used fit range. The blue band indicates the restricted fit range used for the $^{80}Sr^{19}F$ peak analysis. Middle: unbinned time-of-flight data used to perform the mass evaluation. The red vertical bars represent the uncertainty of the mean of the time-of-flight distributions at the $\pm1\sigma$ confidence level. An overview of the experimental data can be found in Methods. Bottom: $\Delta_{2n}(Z,N_0)$ as a function of Z for $N_0=28$ and $N_0=50$ (open grey symbols). The filled grey symbols show the corresponding value of the quantity $\Delta_{2n}(Z,N_0+2)$. At $Z=50$, the filled red circle corresponds to the value of $\Delta_{2n}(Z,N_0+2)$ calculated using the masses from this work and the β-decay energy from ref. [4] and the open blue circle uses the value from ref. [5]. The inset shows a 2.5-fold magnification of the $\Delta_{2n}(Z,N_0+2)$ curve from $Z=44$ to 50. The error bars represent 1 s.d. The dashed vertical lines indicate the magic proton numbers 20, 28 and 50.

is shown in Fig. 2 for illustration. Our data allows extending $\Delta_{2n}(Z,N_0+2)$ to $Z=49$ (indium) and indicates a slight downward trend towards $Z=50$ (Fig. 2 inset), as expected for a doubly magic ^{100}Sn. Eliminating the contribution of the ^{100}In ground-state mass uncertainty in the calculation of the ^{100}Sn mass directly allows to confront the nuclear-structure implications of the two Q-values from refs. [4,5], and a global picture now emerges for this region. As shown, the Q-value reported by Lubos et al.[5] yields a ^{100}Sn mass value that is at odds with the expected trend of $\Delta_{2n}(Z,N_0+2)$ to $Z=49$ (open blue circle in the bottom panel of Fig. 2), whereas the value of Hinke et al.[4] yields a ^{100}Sn mass that agrees with the trend within experimental uncertainties and is in line with our observation for $Z=49$. In other words, while the Q-value reported in ref. [4] follows the expectation of a doubly magic ^{100}Sn, the more recent (and higher-statistics) Q-value reported in ref. [5] yields a ^{100}Sn mass value that suggests quite the opposite. Such a conclusion is at odds with ab initio many-body calculations as discussed below.

In recent years, there has been great progress advancing ab initio calculations in medium-mass nuclei[23,24] up to the tin isotopes[2] based on modern nuclear forces derived from chiral effective field theory of the strong interaction. Most ab initio approaches are benchmarked on even–even nuclei, which are considerably simpler to compute, but this excludes from the benchmark effects that are only visible in odd nuclei. Among these are the single-particle states accessible to the unpaired nucleon and their interaction with the states of the even–even core, the blocking effect on pairing correlations and, in the case of odd–odd nuclei, the residual interaction between the unpaired proton and neutron. The latter two give rise to an odd–even staggering (OES) of binding energies, which can be quantified by a three-point estimator. Odd systems thus provide a complementary and stringent testing ground for state-of-the-art theoretical approaches. Among ab initio approaches, the valence-space formulation of the in-medium similarity renormalization group (VS-IMSRG)[25] is able to access a broad range of closed- and open-shell nuclei in the nuclear chart[26]. In addition, we will explore the shell-model coupled-cluster (SMCC) method[27] in this region. Both the VS-IMSRG and coupled-cluster calculations provide access to a broad range of observables, such as ab initio calculations of beta decays—up to ^{100}Sn (ref. [3]). The VS-IMSRG was also recently shown to adequately describe both OES of nuclear masses and charge radii in neutron-rich odd-Z copper ($Z=29$) isotopes[28]. Here we present VS-IMSRG and SMCC results that allow direct comparisons with the odd-Z nuclides adjacent to the iconic ^{100}Sn nucleus.

We have performed cross-shell VS-IMSRG[29] and SMCC calculations using the 1.8/2.0(EM) two-nucleon (NN) and three-nucleon (3N) interactions of ref. [30]. This interaction is fitted to the properties of nuclear systems with only $A=2$, 3 and 4 nucleons (with 3N couplings adjusted to reproduce the triton binding energy and the

Table 1 | Summary of the mass values obtained in this work

Isotope	Half-life (s)	Method	Ref. nuclides	Ratio $r_{ref,x}$ or C_{ToF}	M_E (keV) this work	M_E (keV) literature
^{99}In	3.1(2)	MR-ToF MS	$^{80}Sr^{19}F^+/^{85}Rb^+$	$C_{ToF}=0.50076578(567)$	−61,429(77)	−61,380[a](300[a])
^{100}In	5.83(17)	MR-ToF MS	$^{81}Sr^{19}F^+/^{85}Rb^+$	$C_{ToF}=0.50060677(139)$	−64,187(20)	−64,310(180)
		ToF-ICR	$^{85}Rb^+$	$r_{ref,x}=1.1768824946(283)$	−64,178.2(22)	
^{101g}In	15.1(11)	ToF-ICR	$^{85}Rb^+$	$r_{ref,x}=1.1886042835(590)$	−68,545.4(47)	−68,545(12)
		PI-ICR	$^{82}Sr^{19}F^+$	$r_{ref,x}=1.0000952633(432)$	−68,542.5(69)	
^{101m}In	10[#]	PI-ICR	$^{82}Sr^{19}F^+$	$r_{ref,x}=1.0001023696(659)$	−67,874.5(83)	−67,907(36)

Columns 1–7: isotope, half-life[39], measurement method, reference (Ref.) nuclides used for the calibration, experimental frequency ratio $r_{ref,x}$ or time-of-flight constant C_{ToF}, and the resulting $M_E=M$ (atomic mass) − A (atomic mass number) × u (atomic mass unit) from this work and the literature. The results from AME2016[20] are listed for ^{99,100}In ([a]extrapolated mass value). For ^{101g,m}In, the values are the weighted averages of two recent measurements performed at the FRS Ion Catcher at GSI[11] and at the CSRe in Lanzhou[12]. The atomic-mass values of the reference nuclides are $m(^{85}Rb)=84,911,789.738(5)$ μu, $m(^{81}Sr^{19}F)=99,921,615(3)$ μu, $m(^{82}Sr^{19}F)=100,916,803(6)$ μu (from AME2016). The mass of the $^{80}Sr^{19}F$ reference was also measured during this run with the ToF-ICR technique using ^{85}Rb as reference, yielding a frequency ratio $r_{ref,x}=1.1650090659(365)$; as a result, the corresponding $m(^{80}Sr^{19}F)=98,922,914(3)$ μu was used.

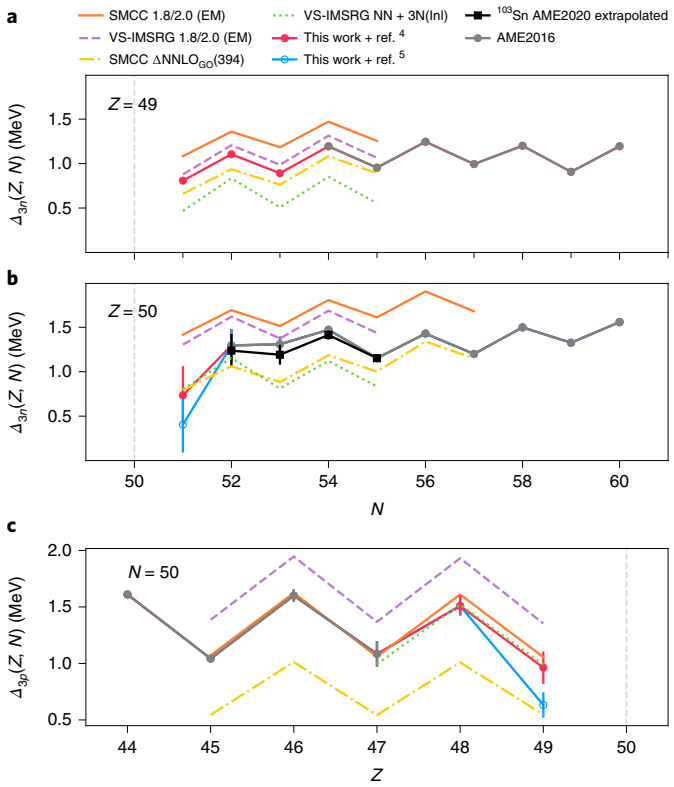

Fig. 3 | Comparison of experimental three-point estimators of the OES with theoretical results. a, Three-point empirical formula of the neutron OES $\Delta_{3n}(Z,N)$ in the indium ($Z=49$) isotopic chain as a function of the neutron number. **b**, Three-point empirical formula of the neutron OES $\Delta_{3n}(Z,N)$ in the tin ($Z=50$) isotopic chain as a function of the neutron number. The solid black line represents the same quantity computed considering the extrapolated ^{103}Sn mass value given in AME2020 (refs. [37,38]). **c**, Three-point empirical formula of the proton OES $\Delta_{3p}(Z,N)$ along the $N=50$ isotonic chain as a function of the proton number. The points resulting from the ^{100}Sn mass deduced with the Q-value from ref. [4] are plotted as the filled red circles while the open blue circles show the value using the ref. [5] Q-value. The error bars represent 1 s.d. The dashed vertical lines indicate the magic proton/neutron number 50.

^{4}He charge radius), and gives accurate results for ground-state energies of light and medium-mass nuclei[26,31]. To further explore the sensitivity to chiral effective field theory interactions, we also consider the NN + 3N(lnl) interaction[32] that has proven to constitute a valuable addition to existing chiral Hamiltonians in medium-mass nuclei[33] but has yet to be tested in heavier systems. Finally, we show results for the ^{100}Sn region with the ΔNNLO$_{GO}$(394) interaction[34]. Calculations with the ΔNNLO$_{GO}$(394) interaction and NN + 3N(lnl) were performed using the SMCC and VS-IMSRG methods, respectively. Technical details regarding these computations can be found in Methods.

Figure 3a presents the experimental three-point empirical formula of the OES, $\Delta_{3n}(Z,N)=0.5\times(-1)^N[M_E(Z,N-1)-2M_E(Z,N)+M_E(Z,N+1)]$ for the odd-Z indium isotopic chain. Figure 3a also shows the trends of $\Delta_{3n}(Z,N)$ calculated with the ab initio methods described above. Both many-body methods using the 1.8/2.0 (EM) interaction yield $\Delta_{3n}(Z,N)$ trends that agree with our experimental results. The differences between the two methods are within estimated theoretical uncertainties (see Methods for details). Calculations performed with the ΔNNLO$_{GO}$(394) and NN + 3N(lnl) interactions slightly underestimate the energy but closely follow the experimental trend, like the more explored 1.8/2.0 (EM) interaction. All in all, the predictions vary with the choice of many-body method and nuclear Hamiltonian in a range of 500 keV, but with all methods yielding excellent trends.

Figure 3b shows the experimental trend of $\Delta_{3n}(Z,N)$ for the tin chain (solid grey line). The experimental $N=53$ point in Fig. 3b deviates from the regular odd–even behaviour of the three-point empirical formula of the OES. This deviation is most likely explained by the AME2016 (ref. [20]) ^{103}Sn mass, which is known indirectly via its β-decay link to ^{103}In (refs. [35,36]). In fact, in the latest version of the Atomic-Mass Evaluation (AME2020)[37,38], this experimental mass value was found to violate the smoothness of the mass surface in this region to such a degree that the evaluators recommended replacing its value by an extrapolated value. The $\Delta_{3n}(Z,N)$ trend for the tin chain obtained with the ^{103}Sn AME2020 extrapolated value (solid black line in Fig. 3b) appears more regular and is better reproduced by the various theoretical calculations. Hence, as for $Z=49$, in $Z=50$ the relative agreement of the theoretical predictions with experiment is good overall. The successful benchmarking of the ab initio calculations by our indium masses gives confidence in their predictions towards ^{100}Sn, only one nucleon away. At $N=51$, the discrepancy observed between the Q-values reported in refs. [4,5] is again highlighted, with that of ref. [4] more in line with our theoretical results. Since the uncertainties of the light tin masses are not as stringent as our indium results, we also compare our predictions with the three-point proton OES as a function of proton number in Fig. 3c. Again, our calculations agree with the experimental trend all the way up to $Z=48$, yielding a staggering of similar magnitude and differing only in absolute values. At $Z=49$ the evolution of all theoretical trends clearly favours the Hinke et al.[4] Q-value over that of Lubos et al.[5].

Online content

Any methods, additional references, Nature Research reporting summaries, source data, extended data, supplementary information, acknowledgements, peer review information; details of author contributions and competing interests; and statements of data and code availability are available at https://doi.org/10.1038/s41567-021-01326-9.

Received: 29 January 2021; Accepted: 14 July 2021;
Published online: 23 September 2021

References

1. Faestermann, T., Górska, M. & Grawe, H. The structure of ^{100}Sn and neighbouring nuclei. *Prog. Part. Nucl. Phys.* **69**, 85–130 (2013).
2. Morris, T. D. et al. Structure of the lightest tin isotopes. *Phys. Rev. Lett.* **120**, 152503 (2018).
3. Gysbers, P. et al. Discrepancy between experimental and theoretical β-decay rates resolved from first principles. *Nat. Phys.* **15**, 428–431 (2019).
4. Hinke, C. B. et al. Superallowed Gamow–Teller decay of the doubly magic nucleus ^{100}Sn. *Nature* **486**, 341–345 (2012).
5. Lubos, D. et al. Improved value for the Gamow–Teller strength of the ^{100}Sn β-decay. *Phys. Rev. Lett.* **122**, 222502 (2019).
6. Jones, K. L. et al. The magic nature of ^{132}Sn explored through the single-particle states of ^{133}Sn. *Nature* **465**, 454–457 (2010).
7. Lewitowicz, M. et al. Identification of the doubly-magic nucleus ^{100}Sn in the reaction ^{112}Sn + ^{nat}Ni at 63 MeV/nucleon. *Phys. Lett. B* **332**, 20–24 (1994).
8. Sümmerer, K. et al. Identification and decay spectroscopy of ^{100}Sn at the GSI projectile fragment separator FRS. *Nucl. Phys. A* **616**, 341–345 (1997).
9. Park, J. et al. β-decays of the heaviest $N=Z-1$ nuclei and proton instability of ^{97}In. *Phys. Rev. C* **97**, 051301(R) (2018).
10. Park, J. et al. New and comprehensive β- and βp-decay spectroscopy results in the vicinity of ^{100}Sn. *Phys. Rev. C* **99**, 034313 (2019).
11. Hornung, C. et al. Isomer studies in the vicinity of the doubly-magic nucleus ^{100}Sn: observation of a new low-lying isomeric state in ^{97}Ag. *Phys. Lett. B* **802**, 135200 (2020).
12. Xu, X. et al. Masses of ground and isomeric states of ^{101}In and configuration-dependent shell evolution in odd-A indium isotopes. *Phys. Rev. C* **100**, 051303(R) (2019).
13. Plettner, C. et al. β-decay of ^{100}In. *Phys. Rev. C* **66**, 044319 (2002).

14. Fedosseev, V. et al. Ion beam production and study of radioactive isotopes with the laser ion source at ISOLDE. *J. Phys. G* **44**, 084006 (2017).
15. Mukherjee, M. et al. ISOLTRAP: an on-line Penning trap for mass spectrometry on short-lived nuclides. *Eur. Phys. J. A* **35**, 1–29 (2008).
16. Herfurth, F. et al. A linear radiofrequency ion trap for accumulation, bunching, and emittance improvement of radioactive ion beams. *Nucl. Instrum. Methods Phys. Res. A* **469**, 254–275 (2001).
17. Wolf, R. N. et al. ISOLTRAP's multi-reflection time-of-flight mass separator/spectrometer. *Int. J. Mass Spectrom.* **349**, 123–133 (2013).
18. Eliseev, S. et al. A phase-imaging technique for cyclotron-frequency measurements. *Appl. Phys. B* **114**, 107–128 (2014).
19. Manea, V. et al. First glimpse of the $N=82$ shell closure below $Z=50$ from masses of neutron-rich cadmium isotopes and isomers. *Phys. Rev. Lett.* **124**, 92502 (2020).
20. Wang, M. et al. The AME2016 atomic mass evaluation (II). Tables, graphs and references. *Chin. Phys. C* **41**, 030003 (2017).
21. Schmidt, K.-H. & Vermeulen, D. in *Atomic Masses and Fundamental Constants 6* (eds Nolen, J. A. & Benenson, W.) 119–128 (Springer, 1980); https://doi.org/10.1007/978-1-4684-3716-4_13
22. Welker, A. et al. Binding energy of ^{79}Cu: probing the structure of the doubly magic ^{78}Ni from only one proton away. *Phys. Rev. Lett.* **119**, 192502 (2017).
23. Wienholtz, F. et al. Masses of exotic calcium isotopes pin down nuclear forces. *Nature* **498**, 346–349 (2013).
24. Garcia Ruiz, R. F. et al. Unexpectedly large charge radii of neutron-rich calcium isotopes. *Nat. Phys.* **12**, 594–598 (2016).
25. Stroberg, S. R. et al. Nucleus-dependent valence-space approach to nuclear structure. *Phys. Rev. Lett.* **118**, 032502 (2017).
26. Stroberg, S. R., Holt, J. D., Schwenk, A. & Simonis, J. Ab initio limits of atomic nuclei. *Phys. Rev. Lett.* **126**, 022501 (2021).
27. Sun, Z. H., Morris, T. D., Hagen, G., Jansen, G. R. & Papenbrock, T. Shell-model coupled-cluster method for open-shell nuclei. *Phys. Rev. C* **98**, 054320 (2018).
28. de Groote, R. P. et al. Measurement and microscopic description of odd–even staggering of charge radii of exotic copper isotopes. *Nat. Phys.* **16**, 620–624 (2020).
29. Miyagi, T., Stroberg, S. R., Holt, J. D. & Shimizu, N. Ab initio multishell valence-space Hamiltonians and the island of inversion. *Phys. Rev. C* **102**, 034320 (2020).
30. Hebeler, K., Bogner, S. K., Furnstahl, R. J., Nogga, A. & Schwenk, A. Improved nuclear matter calculations from chiral low-momentum interactions. *Phys. Rev. C* **83**, 31301 (2011).
31. Simonis, J., Stroberg, S. R., Hebeler, K., Holt, J. D. & Schwenk, A. Saturation with chiral interactions and consequences for finite nuclei. *Phys. Rev. C* **96**, 14303 (2017).
32. Somà, V., Navrátil, P., Raimondi, F., Barbieri, C. & Duguet, T. Novel chiral Hamiltonian and observables in light and medium-mass nuclei. *Phys. Rev. C* **101**, 14318 (2020).
33. Mougeot, M. et al. Examining the $N=28$ shell closure through high-precision mass measurements of $^{46-48}$Ar. *Phys. Rev. C* **102**, 14301 (2020).
34. Jiang, W. G. et al. Accurate bulk properties of nuclei from $A=2$ to ∞ from potentials with Δ isobars. *Phys. Rev. C* **102**, 54301 (2020).
35. Mukha, I. et al. Studies of β-delayed proton decays of $N\simeq Z$ nuclei around ^{100}Sn at the GSI-ISOL facility. *Nucl. Phys. A* **746**, 66–70 (2004).
36. Kavatsyuk, O. et al. Beta decay of ^{103}Sn. *Eur. Phys. J. A* **25**, 211–222 (2005).
37. Huang, W. J., Wang, M., Kondev, F. G., Audi, G. & Naimi, S. The AME 2020 atomic mass evaluation (I). Evaluation of input data, and adjustment procedures. *Chin. Phys. C* **45**, 30002 (2021).
38. Wang, M., Huang, W. J., Kondev, F. G., Audi, G. & Naimi, S. The AME 2020 atomic mass evaluation (II). Tables, graphs and references. *Chin. Phys. C* **45**, 30003 (2021).
39. Audi, G., Kondev, F. G., Wang, M., Huang, W. J. & Naimi, S. The NUBASE2016 evaluation of nuclear properties. *Chin. Phys. C* **41**, 030001 (2017).

Methods

MR-ToF MS mass measurement and analysis. The relation between the time of flight t of a singly charged ion of interest and its mass m_{ion} is given by $t = a(m_{ion})^{1/2} + b$ where a and b are device-specific calibration parameters. These can be determined from the measured flight times $t_{1,2}$ of two reference ions with well known masses $m_{ion,1}$ and $m_{ion,2}$. From the time-of-flight information of all the singly charged species, the mass of an ion is then calculated from the relation $m_{ion}^{1/2} = C_{ToF}\Delta_{ref} + 0.5\Sigma_{ref}$ with $\Delta_{ref} = m_{ion,1}^{1/2} - m_{ion,2}^{1/2}$, $\Sigma_{ref} = m_{ion,1}^{1/2} + m_{ion,2}^{1/2}$ and $C_{ToF} = [2t - t_1 - t_2]/[2(t_1 - t_2)]$ (ref. [23]).The ions' flight times were recorded with a 100 ps resolution. The peaks corresponding to the indium ions of interest were unambiguously identified by their disappearance when blocking the RILIS lasers. The mean of the time-of-flight distribution corresponding to each ion species was estimated using the unbinned maximum-likelihood method, assuming a Gaussian probability density function (PDF). To cope with the pronounced asymmetries observed in the shape of the time-of-flight distribution, a restricted fit range was used (Fig. 2). The dependence of the time-of-flight fit to these tails was compared with an analysis using the asymmetric PDF from ref. [40]. The difference between the extracted mean time of flight was subsequently treated as a systematic time-of-flight uncertainty and was found to be the dominant contribution in the final uncertainty. When too many ions are trapped in the MR-ToF MS, space-charge effects can cause the time-of-flight difference between two species to shift, affecting the accuracy of the mass determination. To mitigate this effect, the count rate was always kept below 8 ions per cycle, which has proven to be a safe limit from previous tests. Nonetheless, count-rate effects were investigated and were found not to be statistically relevant. In the case of ^{99}In, an additional source of systematic uncertainty was considered. The sensitivity of the extracted time of flight to the presence of a possible isomeric state was studied employing a Monte Carlo approach. We assumed that the ratio of ground and isomeric states for ^{99}In was similar to that observed for ^{101}In (that is, 25:1), because the two states in ^{99}In are expected to have the same spin and parity. Our procedure yields a conservative estimate, since the target release efficiencies (expected to be lower for ^{99}In than ^{101}In due to shorter half-lives) are not taken into account. The result of this study was treated as an additional systematic uncertainty, which was added in quadrature. Note that our MR-ToF MS mass value for ^{100}In is in good agreement with our Penning-trap value (see Table 1).

Principle of Penning-trap mass spectrometry. Penning-trap mass spectrometry relies upon the determination of the free cyclotron frequency $\nu_C = qB/(2\pi m_{ion})$ of an ion species stored in magnetic field B and charge q. Comparing ν_C with the frequency $\nu_{C,ref}$ of a species of well known mass yields the frequency ratio $r_{ref,x} = \nu_{C,ref}/\nu_C$, from which the atomic-mass value of the ion of interest can be directly calculated. For singly charged ions, the atomic mass of the species of interest is thus expressed as $m_{atom} = r(m_{atom,ref} - m_e) + m_e$, where m_e is the electron mass[41]. As contributions from electron binding energies are orders of magnitude smaller than the statistical uncertainty, they are neglected here.

ToF-ICR mass measurements and analysis. The mass of ^{100}In was measured using the well established ToF-ICR technique using both one-pulse excitation[42] and two-pulse, Ramsey-type excitation[43]. In this method, the free cyclotron frequency of an ion is directly determined. From one experimental cycle to the next, the frequency of an excitation pulse is varied. Following this excitation, the ions are ejected from the trap and their time of flight to a downstream microchannel plate detector is measured. The response of the ions to the applied excitation is a resonant process whose resonance frequency is ν_C and for which a minimum of the time of flight is observed. In the Ramsey scheme, two excitation pulses coherent in phase and separated by a waiting time are applied. The measured Ramsey-type ToF-ICR resonance for ^{100}In is shown in Extended Data Fig. 1a. For the same total excitation time, this method offers a threefold precision improvement when compared with the single-pulse ToF-ICR method. In both cases, the analysis was performed using the EVA analysis software and the various sources of systematic uncertainties were treated according to ref. [44]. A mass value for ^{101}In was likewise measured and agrees with a value determined by PI-ICR (see below) within one combined s.d.

PI-ICR mass measurements and analysis. To separate the $A = 101$ isomers, the recently introduced PI-ICR technique was used[18]. With this method, the radial frequency of ions prepared on a pure cyclotron or magnetron orbit is determined through the measurement of the phase they accumulate in a time t_{acc} using the projection of their motion onto a position-sensitive multichannel plate detector. The PI-ICR technique offers several advantages over the regular ToF-ICR technique. First, it is a non-scanning technique, which greatly reduces the number of ions required to perform a measurement; that is, only five to ten ions are required, where a minimum of 50–100 are required for ToF-ICR. While the resolving power of the ToF-ICR method is entirely limited by the excitation time, the resolving power of PI-ICR depends on the observation time and the ion-distribution spot size projected on the detector.

A three-step measurement scheme allows for the direct determination of ν_C. First, a position measurement is performed without preparing the ions on a specific motion radius, yielding the position of the centre of the ions' motion. In a second step, the ions are prepared on a pure magnetron orbit, left to evolve freely during a time t_{acc} and their position measured. Finally, the ions are prepared on a pure reduced cyclotron orbit, left to evolve freely during the same time t_{acc} and their position again measured. The integer number of revolutions n_- and n_+ performed in steps 2 and 3 respectively, t_{acc} and the angle Φ between the ions' positions obtained in steps 2 and 3 can be related to ν_C following the relation $\nu_C = [2\pi(n_- + n_+) + \Phi]/t_{acc}$. In step 3, the phase accumulation is performed at the modified cyclotron frequency, so is mass dependent. The position of each ion spot was extracted using the unbinned maximum-likelihood method, assuming a two-dimensional multivariate Gaussian distribution[45]. Extended Data Figure 1 shows a typical PI-ICR image obtained in step 3 after ~62 ms of phase accumulation. As in principle the angle $\Phi_{gs,m}$ between the ground and isomeric states directly reflects the energy difference between the two states, the mass of each state was measured separately to mitigate systematical effects. The PI-ICR method was used to study the isomeric composition of the ^{100}In beam. Hence, we can exclude the presence of a long-lived state with an excitation energy higher than 20 keV in the ^{100}In beam delivered to ISOLTRAP's measurement Penning trap.

VS-IMSRG calculations. The VS-IMSRG calculations[25,46] were performed in a spherical harmonic-oscillator basis including up to 15 major shells in the single-particle basis with an oscillator frequency $\hbar\omega = 16$ MeV. The 3N interaction configurations were restricted up to $e_1 + e_2 + e_3 \leq E_{3max} = 16$ for the 1.8/2.0 (EM) interaction (to compare with SMCC calculations) and $E_{3max} = 22$ for the NN + 3N(lnl) interaction. We first transform to the Hartree–Fock basis, then use the Magnus formulation of the IMSRG[47] to construct an approximate unitary transformation to decouple a ^{78}Ni core with a proton $p_{1/2}$, $p_{3/2}$, $f_{5/2}$, $g_{9/2}$ and neutron $s_{1/2}$, $d_{3/2}$, $d_{5/2}$, $g_{7/2}$, $h_{11/2}$ valence space. Using the ensemble normal ordering introduced in ref. [25], we approximately include effects of 3N interactions between valence nucleons, such that a specific valence-space Hamiltonian is constructed for each nucleus to be studied. The final diagonalization is performed using the KSHELL shell-model code[48]. To estimate theoretical uncertainties in this framework, we note that in the limit of no IMSRG truncations the results would be independent of the chosen reference state for the ensemble normal ordering procedure. Therefore, we examine the reference-state dependence of the observables discussed above. For normal ordering with respect to either a filled neutron $g_{7/2}$ or $d_{5/2}$ orbit, we find approximately 1 MeV uncertainty for absolute or one-neutron separation energies. However, for all quantities shown in Fig. 3, this estimated uncertainty is approximately 0.1 MeV.

SMCC calculations. The SMCC approach generates effective interactions and operators through the decoupling of a core from a valence space. We start from a single Hartree–Fock ^{100}Sn reference state, computed in a harmonic-oscillator basis comprising up to 11 major oscillator shells and $\hbar\omega = 16$ MeV. The 3N interaction was restricted to $E_{3max} = 16\hbar\omega$. The doubly closed-shell ^{100}Sn core is decoupled by coupled-cluster calculations including single, double and the leading-order triple excitations (CCSDT-1 approximation). We note that triple excitations were performed in the full model space, without any truncations. This work was made possible by employing the Nuclear Tensor Contraction Library (NTCL)[49] developed to run at scale on Summit, the US Department of Energy's 200 petaflop supercomputer operated by the Oak Ridge Leadership Computing Facility (OLCF) at Oak Ridge National Laboratory. The SMCC calculations then proceed via a second similarity transformation that decouples a particle–hole valence space defined by the proton $pfg_{9/2}$ holes and neutron $g_{7/2}sd$ single-particle states. The SMCC decoupling only includes the one- and two-body parts of the CCSDT-1 similarity-transformed Hamiltonian. To estimate theoretical uncertainties, we note that the calculation of doubly magic nuclei such as ^{100}Sn or ^{78}Ni and their neighbours is ideally suited for the coupled-cluster method, because the reference state is closed shell[2,46]. Comparison of the SMCC results for ^{101}Sn with those from ref. [2] exhibit differences in single-particle energies of about 0.2 MeV. We therefore estimate that our theoretical uncertainties on $\Delta_{3n}(Z,N)$ are about ±0.2 MeV.

Data availability

Source data are provided with this paper.

Code availability

The analysis codes used for the ToF-ICR and MR-ToF MS data are available from the corresponding author upon reasonable request. A second MR-ToF MS analysis code used in this study is available at https://github.com/jonas-ka/mr-tof-analysis. The PI-ICR analysis code[45] used in this study is available at https://github.com/jonas-ka/pi-icr-analysis. The code used for the VS-IMSRG calculations is available at https://github.com/ragnarstroberg/imsrg. The source code of KSHELL is available in ref. [48].

References

40. Lan, K. & Jorgenson, J. W. A hybrid of exponential and Gaussian functions as a simple model of asymmetric chromatographic peaks. *J. Chromatogr. A* **915**, 1–13 (2001).

41. Sturm, S. et al. High-precision measurement of the atomic mass of the electron. *Nature* **506**, 467–470 (2014).
42. König, M., Bollen, G., Kluge, H. J., Otto, T. & Szerypo, J. Quadrupole excitation of stored ion motion at the true cyclotron frequency. *Int. J. Mass Spectrom. Ion Process.* **142**, 95–116 (1995).
43. George, S. et al. Ramsey method of separated oscillatory fields for high-precision Penning trap mass spectrometry. *Phys. Rev. Lett.* **98**, 162501 (2007).
44. Kellerbauer, A. et al. From direct to absolute mass measurements: a study of the accuracy of ISOLTRAP. *Eur. Phys. J. D* **22**, 53–64 (2003).
45. Karthein, J. jonas-ka/pi-icr-analysis. *Zenodo* https://doi.org/10.5281/zenodo.3965767 (2020).
46. Stroberg, S. R., Hergert, H., Bogner, S. K. & Holt, J. D. Nonempirical interactions for the nuclear shell model: an update. *Annu. Rev. Nucl. Part. Sci.* **69**, 307–362 (2019).
47. Morris, T. D., Parzuchowski, N. M. & Bogner, S. K. Magnus expansion and in-medium similarity renormalization group. *Phys. Rev. C* **92**, 34331 (2015).
48. Shimizu, N., Mizusaki, T., Utsuno, Y. & Tsunoda, Y. Thick-restart block Lanczos method for large-scale shell-model calculations. *Comput. Phys. Commun.* **244**, 372–384 (2019).
49. Jansen, G. NTCL—Nuclear Tensor Contraction Library. *GitLab* https://gitlab.com/ntcl/ntcl (2021).

Acknowledgements

We thank the ISOLDE technical group and the ISOLDE Collaboration for their support. We acknowledge the support of the Max Planck Society, the French Institut National de Physique Nucléaire et de Physique des Particules (IN2P3), the European Research Council (ERC) through the European Union's Horizon 2020 research and innovation programme (grant agreement 682841 'ASTRUm' and 654002 'ENSAR2') and the Bundesministerium für Bildung und Forschung (BMBF; grants 05P15ODCIA, 05P15HGCIA, 05P18HGCIA and 05P18RDFN1). J.K. acknowledges the support of a Wolfgang Gentner PhD scholarship from the BMBF (05E12CHA). This work was supported by the US Department of Energy, Office of Science, Office of Nuclear Physics, under awards DE-FG02-96ER40963 and DE-FG02-97ER41014. This material is based upon work supported by the US Department of Energy, Office of Science, Office of Advanced Scientific Computing Research and Office of Nuclear Physics, Scientific Discovery through Advanced Computing (SciDAC) programme under award DE-SC0018223. TRIUMF receives funding via a contribution through the National Research Council of Canada, with additional support from NSERC. Computer time was provided by the Innovative and Novel Computational Impact on Theory and Experiment (INCITE) Program. This research used resources of the Oak Ridge Leadership Computing Facility located at Oak Ridge National Laboratory, which is supported by the Office of Science of the Department of Energy under contract DE-AC05-00OR22725. The VS-IMSRG computations were performed with an allocation of computing resources on Cedar at WestGrid and Compute Canada, and on the Oak Cluster at TRIUMF managed by the University of British Columbia department of Advanced Research Computing (ARC). R.N.W. acknowledges support by the Australian Research Council under the Discovery Early Career Researcher Award scheme (DE190101137).

Author contributions

M.M., D.A., J.K., P.A., I.K., Y.A.L., V.M., T.S., A.W. and F.W. performed the experiment. M.M., D.A., J.K. and R.N.W. performed the data analysis. K.C. and S.G.W. set up the resonant laser ionization scheme. W.J.H. performed the update of the Atomic-Mass Evaluation with the latest experimental results. G.H., J.D.H., G.R.J., T.M., T.P., S.R.S. and Z.H.S. performed the theoretical calculations. K.B., V.M., D.L., A.S., L.S., K.Z. and M.M. prepared the manuscript. All authors discussed the results and contributed to the manuscript at all stages.

Competing interests

The authors declare no competing interests.

Additional information

Extended data is available for this paper at https://doi.org/10.1038/s41567-021-01326-9.

Supplementary information The online version contains supplementary material available at https://doi.org/10.1038/s41567-021-01326-9.

Correspondence and requests for materials should be addressed to M. Mougeot.

Peer review information *Nature Physics* thanks Nunzio Itaco and the other, anonymous, reviewer(s) for their contribution to the peer review of this work.

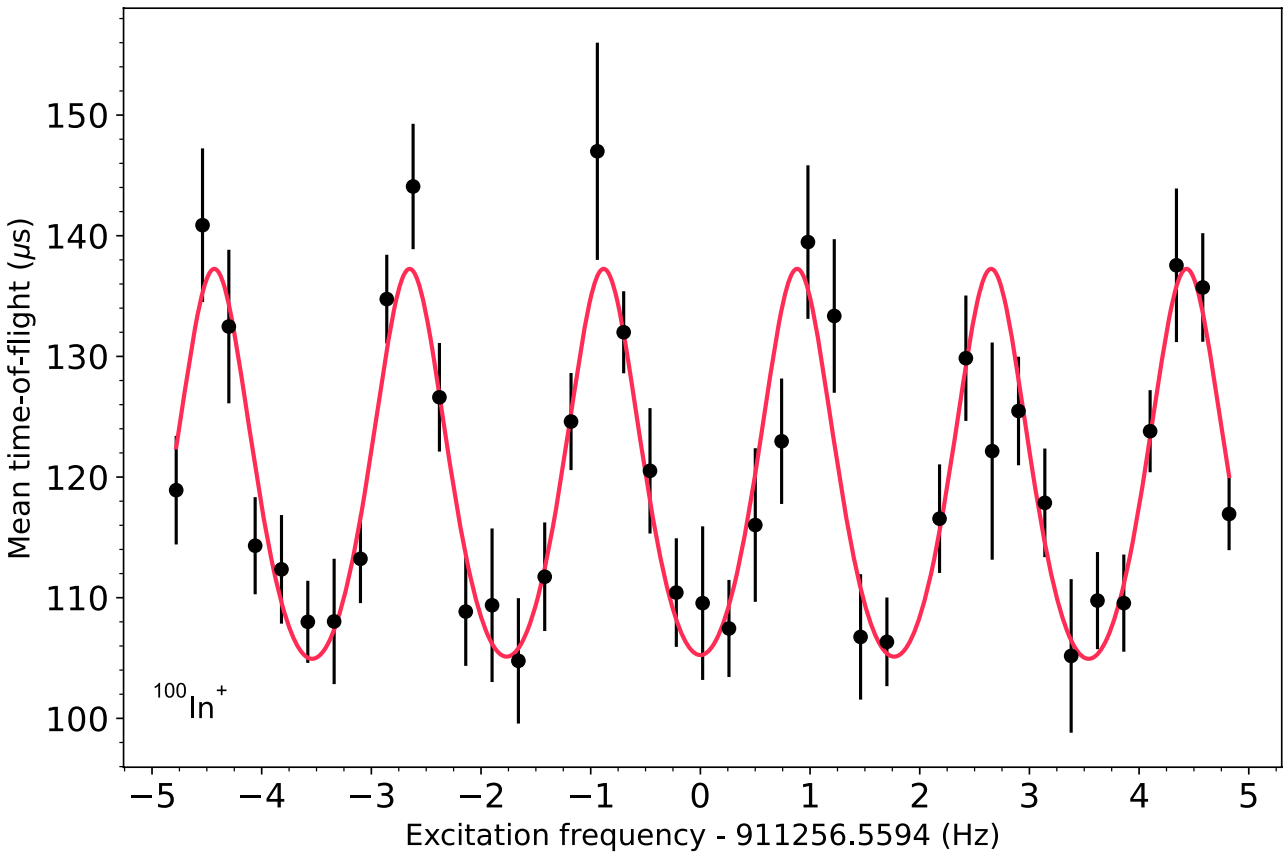

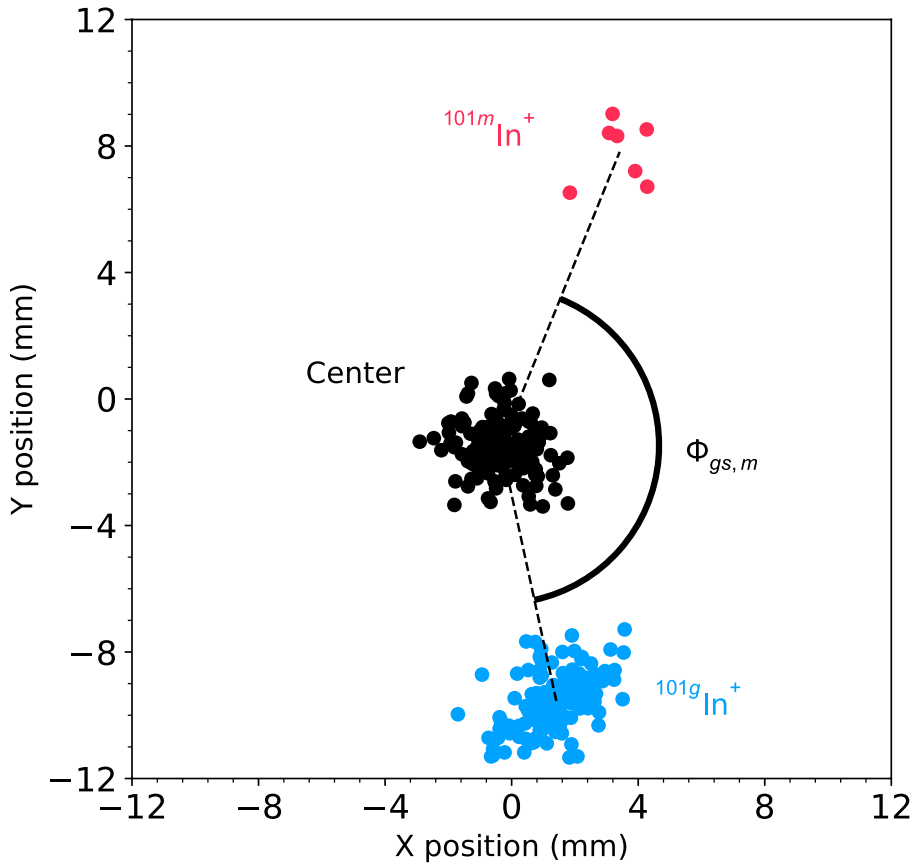

Extended Data Fig. 1 | See next page for caption.

Extended Data Fig. 1 | Overview of experimental results (continued). (**a**), Ramsey ToF-ICR resonance of $^{100}In^{+}$ containing about 160 ions. A Ramsey pattern of T_{RF}^{on}-T_{RF}^{off}-T_{RF}^{on} = 50 ms – 500 ms – 50 ms was used for this measurement. The solid red line corresponds to the least-square adjustment of the theoretical line shape to the data. (**b**), PI-ICR ion-projection image of $^{101}In^{+}$. (0,0) marks the center of the position sensitive detector. In a phase-accumulation of about 62 ms a mass resolving power in excess of 5.10^5 was reached allowing for the ground (blue) and isomeric (red) states to be separated by the angle $\Phi_{gs,m}$ which directly determines the nuclear excitation energy. The centre (black) of the projected ion motion is obtained in a separate measurement. The error bars represent one standard deviation.